Characterization of biodegradable core–clad borosilicate glass fibers with round and rectangular cross-section

Mikko Hongisto, Sonya Ghanavati, Arnaud Lemiere, Gregory Hauss, Shashank Boraiah, Louis Cornet, Angeline Poulon-Quintin, Dominique Pagnoux, Dominique Bernard, Jonathan Massera, et al.

Characterization of biodegradable core-clad borosilicate glass fibers with round and rectangular cross-section

Mikko Hongisto[1,2], Sonya Ghanavati[2,3], Arnaud Lemiere[2], Gregory Hauss[4], Shashank Boraiah[1], Louis Cornet[1], Angeline Poulon-Quintin[1], Dominique Pagnoux[5], Dominique Bernard[1], Jonathan Massera[3], Laeticia Petit[2], Veronique Jubera[1], Sylvain Danto[1]*

[1] Univ. Bordeaux, CNRS, Bordeaux INP, ICMCB, UMR 5026, Pessac, F-33600, France

[2] Tampere University, Photonics Laboratory, Korkeakoulunkatu 3, Tampere, FI-33720, Finland

[3] Tampere University, Faculty of Medicine and Health Technology, Tampere, FI-33720, Finland

[4] Univ. Bordeaux, CNRS, PLACAMAT, UMS 3626, Pessac, F-33600, France

[5] Univ. de Limoges, XLIM, UMR CNRS 7252, 123 Avenue A. Thomas, Limoges, F-87060, France

Keywords: Fibers; Borosilicate glass; Bioactive glass; Biodegradation

Corresponding author* sylvain.danto@u-bordeaux

Abstract

Here we report on core-clad bioactive borosilicate fibers, that we have prepared both with round and rectangular cross-section profile. The exposed approach, which relies on the stacking and drawing of glass slabs, demonstrates our ability to develop bioactive-based glass fibers with tailored cross-section profiles. Tens-of-meters-long fibers were successfully drawn, although suffering from elevated losses in the case of the rectangular ones. The response of the fibers in simulated body fluid was studied for both geometries. We found that a round cladding can act as protective layer, tempering effects of the corrosion. We also noticed that rectangular fibers are more prone to degradation, the enhanced corrosion beginning from their sharp corners as they accumulated residual tensile stress during drawing. To the best of our knowledge, this is the first report on the effect of residual tensile stresses from surface tension deformations applied to the corrosion of rectangular fibers. As geometry plays a critical role on the biodegradation behavior of the fiber glass, we believe the enclosed results could lead to the design of fiber devices with tailored cross-section profile in order to tune their rate of degradation on solely-based geometrical effects.

Introduction

The manufacturing of advanced optical waveguides by joining multiple premade components into a preform and by drawing this preform into a microstructured optical fiber was introduced in the late 1980s.[1, 2] Progress on the so-called stack-and-drawn method enabled for the manufacturing of fibers of arbitrary shape, ultimately leading to the advent of photonic crystal fibers.[3-6] So far, due to fabrication constraints, the overall fiber external profiles (not accounting fiber core profiles) have been overwhelmingly circular.

Recently, refinement of the stack-and-draw method enabled new innovations such as metallic nanowires for near field optics or plasmonics,[7] or multimaterial ribbon fibers with metallic electrodes for electrical arc plasma spectroscopy.[8] In the latter case, demonstration of complex non-cylindrical fiber cross section based on fused soda-lime glass blocks was performed.

In the meantime, the use of microstructured guiding optical fibers has received increasing attention, such as exposed core silica fiber for the detection of zinc ions,[9] or plasmonics sensors based on fused silica photonic crystal fibers.[10] Other studies have covered the use of multicore fibers as endoscopes.[11, 12] Nevertheless, few studies to date have explored the potential for bioactive glasses combined with the stack-and-draw method. For reference, bioactive glasses form a subset of glasses that offer biological compatibility with the human body, such as no rejection mechanisms and absorption into the human body. Such glasses have the potential to favor osteogenesis to assist in bone tissue regeneration.[13] Among the reported achievements Gallichi-Nottiani *et al.*[14] prepared a microstructured bioresorbable fiber by first extruding phosphate glass capillaries and then fusing the capillaries together during drawing, demonstrating the use of bioresorbable glass in microstructured fibers. Rizi *et al.*[15] demonstrated combined guiding of a laser beam in a core-clad fiber and of a fluid in a capillary, both guides being made from bioresorbable materials stacked in a single circular fiber.

Despite such advances, no polygonal fibers have been explored yet in the context of bioactive fibers. In the current manuscript we propose to study the potentials that the stack-and-draw method offers to the design of bioactive optical fibers with unusual cross-section shapes, with the objective to put

light on the constraints, advantages and challenges such design may pose in comparison with round fibers. To efficiently treat our research endeavor, we selected the most suitable materials for the targeted application in the SiO_2-B_2O_3-Na_2O-P_2O_5-CaO borosilicate system, the composition of which was tuned with ytterbium oxide to adjust its thermal, rheological and optical properties while providing emission at ~1 µm. Then original manufacturing protocols, both for round and rectangular core-clad fibers, were developed. Following extended characterization of the glass bulks and fiber parts were performed, involving Raman spectroscopy together with absorption and fluorescence spectroscopies, X-ray tomography, electronic microscopy and fiber loss measurement. Finally, we followed and compared the optical properties of the elaborated core-clad fibers, in round and rectangular shapes, while immersed in simulated body fluid (SBF).

Methods

i. Glass preparation and characterization

Glasses with nominal composition (100-*x*)(26.93 SiO_2 – 26.93 B_2O_3 – 22.66 Na_2O – 1.72 P_2O_5 – 21.76 CaO) – *x* Yb_2O_3 in mol-% with *x* = 0, 0.25, 0.50, 0.75, 1.00 and 1.25% were prepared from high-purity chemicals. Batches of 25 grams were weighed, mixed and melt in a Pt crucible (SiO_2: 99.5%, Alfa Aesar ; B_2O_3: 99.9%, Merck ; Na_2CO_3 : 100.05% dry basis, Alfa Aesar ; Na_3PO_4 : 96%, Sigma-Aldrich ; $CaCO_3$: 99.9%, Sigma-Aldrich ; Yb_2O_3 : 99.9%, ABCR). The temperature profile consisted in 10 °C/min heating with 30 min holding periods at 400, 850, and 1250 °C for drying, initial fusion and CO_2 release, and fining steps, respectively (furnace Carbolite BLF1700). The glass melts were quenched in preheated molds and annealed at 450 °C (furnace Carbolite CWF1300). Brass molds were used for bulk pieces and graphite for round fiber preforms. The glasses were annealed for 8 hours at *Tg*-100°C before cooling down naturally to room temperature. Finally the glasses were cut to desired shapes and polished (suspensions H_2O/Al_2O_3 15 µm, 9 µm and H_2O/CeO_2 1.5 µm) on laboratory lapping machines from Logitech (UK).

Thermal analysis of the prepared glasses was performed by differential scanning calorimetry (DSC) on powdered glass using DTA 404 PC (Netzsch -Gerätebau, Germany) in Pt-Ir crucibles. The heating rate was set at 10 °C/min in air. The density measurement was performed using Archimedes' principle from the weight of a bulk piece in air and then immersed in diethyl phthalate (*99.5%*, Sigma-Aldrich, Germany) using a Precisa XT220A laboratory balance (Precisa, Switzerland) with the associated density measurement kit. The glass quantity used for density measurement was in the range 0.2 - 0.7g.

Knoop micro-hardness indentation measurement was done on Leica VMHT (Leica Microsystems, Germany) universal hardness tester with a Knoop diamond tip. A 100 grams weight was applied to load the tip for 20 s and the resulting indentation was measured optically from indentation length. In order to estimate possible inhomogeneities, 12 independent measurements were taken from ~2 cm^2 area and averaged for one sample. Surface roughness of the samples was monitored over time by measuring it using a white light interferometer Wyko NT1100 (Veeco, USA) in VGA mode and a 10× magnification.

The refractive index was determined using an Abbe refractometer (ATAGO, Japan) when illuminated with a 589 nm light source. Optical absorption spectrum in the UV-Visible-NIR range was obtained with a Cary 5000 (Agilent, USA) dual path spectrometer. In the infrared range, the measurement was performed using a single path Equinox 55 (Bruker, USA) Fourier Transfer Infrared (FTIR) spectrometer in air scrubbed from water vapors and CO_2. The absorption coefficient $\alpha(\lambda)$ was determined using Equation 1:

$$\alpha(\lambda) = \frac{\ln 10\, A(\lambda)}{L} \quad (1)$$

where $A(\lambda)$ is the absorbance, L is the bulk sample thickness.

NIR emission was measured using an iHR320 (Horiba, Japan) spectrometer with a Xenon arc lamp filtered to 240 nm as the excitation source. The emission spectra were measured from powdered samples with a LN_2 cooled DSS-IGA020L InGaAs detector (Horiba, Japan).

ii. Preforms and fibers fabrication

Fibers were thermally drawn from a macroscopic scaled-up preform, which is elongated through localized thermal heating while being hold vertically. The manufacturing of the round and rectangular core-clad preforms required developing two different original methods (Figure 1). For all geometries the undoped borosilicate glass was selected to form the cladding of the fiber while, in order to provide refractive index contrast and a probing functionality, the glass doped with 1.0 mol-% Yb_2O_3 was selected as the core composition.

To prepare the round cross-section preforms, the undoped glass (cladding) was first cast into a preheated graphite mold, followed by a graphite rod being impinged into the molten glass (Figure 1a). The graphite rod was then immediately pulled out, leaving a cavity to which the Yb-doped core was cast. The resulting preform, still within the graphite mold, was then annealed as a whole. Finally, once back at room temperature, the preform surface was optically polished by abrasive papers to remove residual graphite before drawing. Cylindrical macroscopic glass preform of 8 mm in diameter and ~7 cm in length could be prepared in the manner.

The elaboration of rectangular preforms relied on the stack-and-draw method, as described in Figure 1b. Bulk glass parts were first cut into rectangular parallelepipeds optically polished on the joint sides (averaged sizes: length 6 cm, width: 1 cm, thickness: 0.5 cm). A three-part assembly was stacked at 575 °C for 1 hour under a homogeneous applied pressure of ~100 g cm^{-2}. The stacking step was repeated once more to achieve the final geometry. All four sides were then polished to an optical finish before drawing.

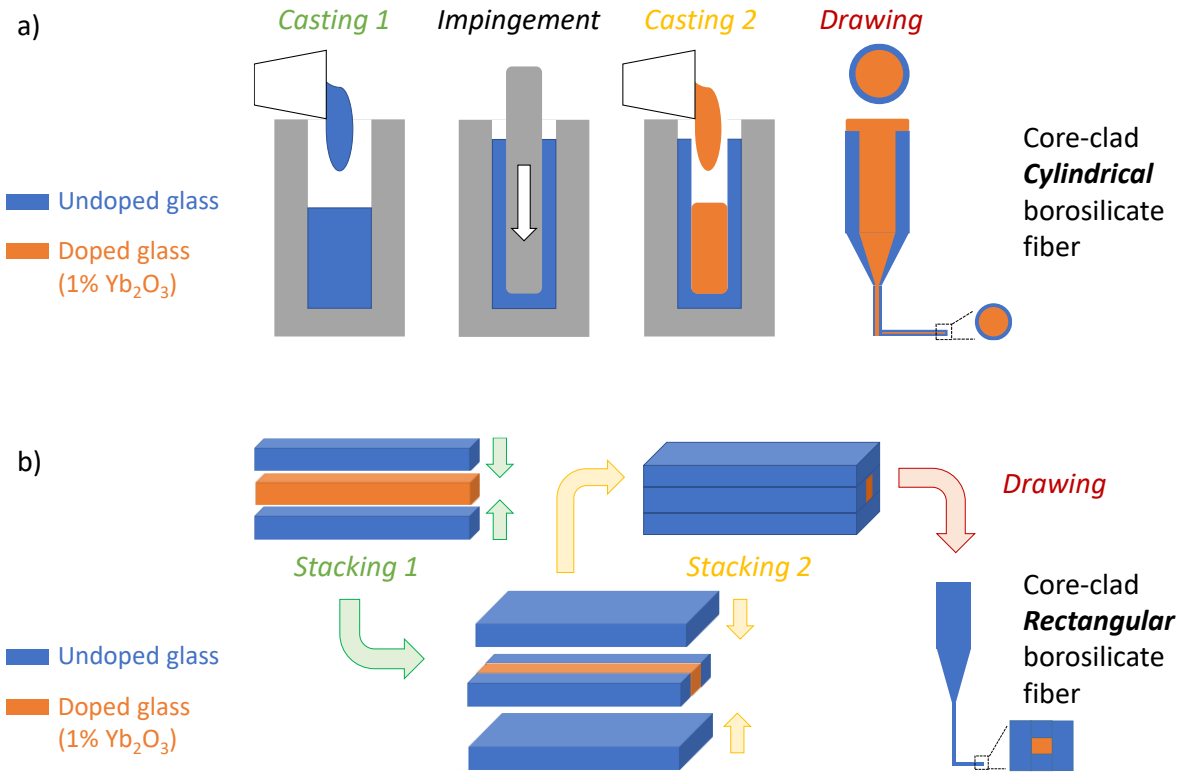

Figure 1: Schematic diagrams of the manufacturing processes for (a) the round core-clad preforms and (b) the rectangular core-clad fiber preforms

The preforms were drawn into fibers at ~600 °C on an optical fiber drawing tower (N.M. Knight Company, USA) under flowing argon atmosphere (3 $L.mn^{-1}$). No coating was applied to the fibers after drawing, as it would interfere in the dissolution test. The preform feed rates, drawing speeds and furnace temperature were adjusted to match with preform dimensions, compositions and geometries, the targeted size being in the order of 400 µm.

iii. Preforms and fibers characterizations

Scanning electron microscope (SEM) Zeiss Crossbeam 540 (Zeiss, Germany) was used in conjunction with energy dispersive spectrometer (EDS) detector X-MaxN 80 (Oxford Instruments, UK) to image and analyze elemental concentration across the face of a rectangular core-clad fiber. TESCAN Vega II SBH SEM (TESCAN, Czech Republic) was used to further image fiber cross-sections.

3D X-ray computational tomography (CT) was performed on GE Phoenix v|tome|x (General Electric, USA) with an approximate voxel size of 2 µm. X-Ray Diffraction (XRD) patterns were measured on powdered samples by means of a PANalytical X'Pert Pro diffractometer (Malvern Panalytical, UK) using the copper Kα radiation on aluminum sample holders. Measurement time was approximately 3h for 2θ angles from 10° to 80°.

Raman spectra were obtained with a LabRAM HR (Horiba, Japan) system, with a stabilized 532 nm excitation source Sapphire SF (Coherent, USA), a 1200 lines.mm^{-1} grating, Synapse 354308 CCD Camera (Horiba, Japan) and a 50× microscope objective in a confocal configuration. The same system was utilized for measuring microluminescence mappings. Here, a stabilized 975 nm laser L4975M-200-TE (Micro Laser Systems, USA) was used with 300 lines.mm^{-1} and a LN_2 cooled Symphony II InGaAs array detector (Horiba, Japan). Furthermore, off-axis scattering of the fiber was mapped by injecting a 980 nm beam from a fiber-coupled laser (Applied Optronics Corp., USA) and imaging the scattered light with the aforementioned camera. Microscope images of the fiber ends were taken with a Leica DMI3000M microscope (Leica Microsystems, Germany) using a 10× objective.

Optical loss in fibers was determined using the cutback method. White light from a halogen light source DH-2000-BAL (Ocean Insight, USA) was launched into a fiber being tested and the transmitted light spectrum was measured with a AvaSpec-ULS4096CL-EVO spectrometer (Avantes, The Netherlands). Fiber coupling was done via butt coupling the fiber ends together. The fiber was shortened by few centimeters and measurements were repeated. The optical absorption in dB at a given wavelength was then plotted as a function of a length of fiber, followed by least squares fit to obtain the loss in dB/m from the fitted slope.

iv. Simulated body fluid on fiber samples

Simulated body fluid (SBF) was prepared in accordance with protocol detailed in [16]. The SBF setup is detailed in Figure 2. For the measurement of evolution of loss of fibers in SBF, a multimode fiber was either connected to a halogen white light source MG922A (Anritsu, Japan) or to a 976 nm single mode pigtailed laser diode CM96Z300-76 (II-VI Photonics, USA) to act as a light source.

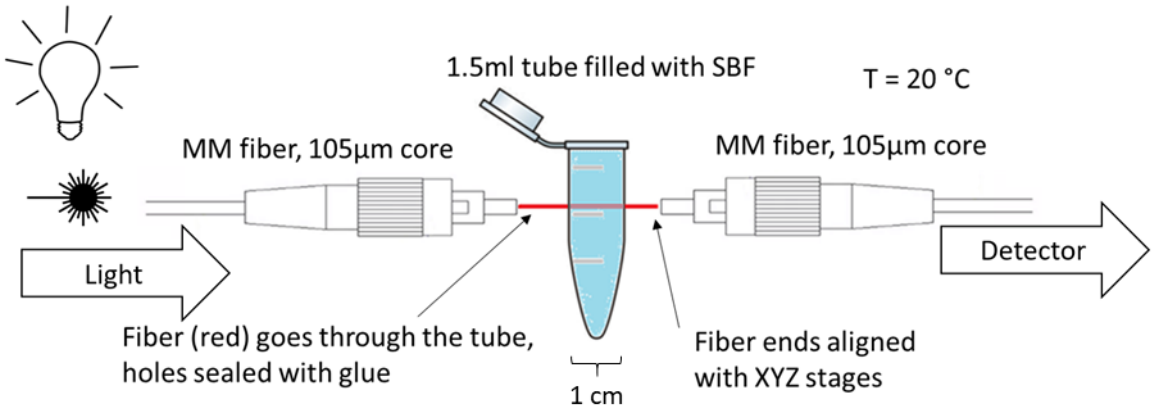

Figure 2: Schematic diagram of the method used to measure transmission loss in SBF

The input fiber was butt coupled with a XYZ stage to the end of a fiber that passed through a 1.5 ml plastic centrifuge tube. Holes through the tube were sealed with PVA glue. The output was collected with another XYZ-stage aligned multimode fiber that was connected to an Ando AQ6317B (Yokogawa, Japan) optical spectrum analyzer (OSA) for measurement. Data was collected at the highest sensitivity setting at 2 nm intervals from 600 to 1600 nm.

Results and Discussion

i. Glass properties

Table 1 depicts selected physical, thermal, optical and spectroscopic properties of the prepared glasses. DSC curves of the investigated glasses are shown in Supplementary Figure S1. The glass transition temperatures (T_g) were determined as local minima of the thermogram first derivatives. T_g values are clearly visible at around 515 °C for all glasses. A thermal signal is detected at around 600°C for all the compositions. To understand its nature, a bulk glass was heated for 36 hours at this temperature, indicating that this event is associated to the peak crystallization (T_p) temperature. On heated powdered glass, $CaNa_3B_5O_{10}$ and $Na_4Ca_4Si_6O_{18}$ were identified as the main crystal phases (Supplementary Figure S2).[17]

Table 1: Selected physical, thermal, optical and spectroscopic properties of glasses

(in blue: fiber core glass, in orange: fiber cladding glass)

Yb_2O_3 (mol-%)	T_g (°C) ± 3 °C	T_p (°C) ± 3 °C	Density (g cm^{-3}) ± 0.02 g cm^{-3}	Refractive index at 589 nm ± 0.001	Knoop hardness (HK 0.1/20)	Yb^{3+} ions (10^{20} ions cm^{-3})	Absorption coefficient at 976 nm (cm^{-1}) ± 10%
0.0 (clad)	518	595	2.62	1.5625	502 ± 28	0.0	0.00
0.25	517	599	2.68	1.5633	-	1.3	1.79
0.50	516	595	2.71	1.5644	-	2.5	3.22
0.75	518	597	2.74	1.5675	-	3.7	4.63
1.0 (core)	513	602	2.77	1.5686	529 ± 22	5.0	6.41
1.25	520	604	2.78	1.5713	-	6.2	8.11

Density of the glasses increases with the concentration of Yb_2O_3, in agreement with previously reported data.[18] Similarly the refractive index increases due to the adding of heavy lanthanide ions as compared to the much lighter ions in the base glass. Increased refractive index is important as it results in larger numerical aperture and then in higher number of guided modes in core-clad fibers. The Knoop microhardness was slightly higher in a doped glass than in the undoped one, in agreement with [19].

The stability of the glasses in air was evaluated by monitoring the evolution of surface roughness and OH-related IR bands. The glasses were stored in ambient air and in vacuum oven at 75°C for several weeks (relative humidity of the locale ambient air in 70-80% range). It was found that no changes in the surface roughness were seen for undoped or 1 mol-% doped glasses for up to 30 days (Supplementary Figure S3a). Furthermore, the IR bands attributed to water [20, 21] did not exhibit meaningful differences for glasses stored in air *versus* vacuum (Figure S3b).

Graphs detailing the optical absorption/emission properties of the glass and Yb^{3+} ions are shown in Figure 3. Figure 3a shows the optical bandgap of the glass at different Yb^{3+} concentrations. Dashed lines are extrapolation to assist the analysis.

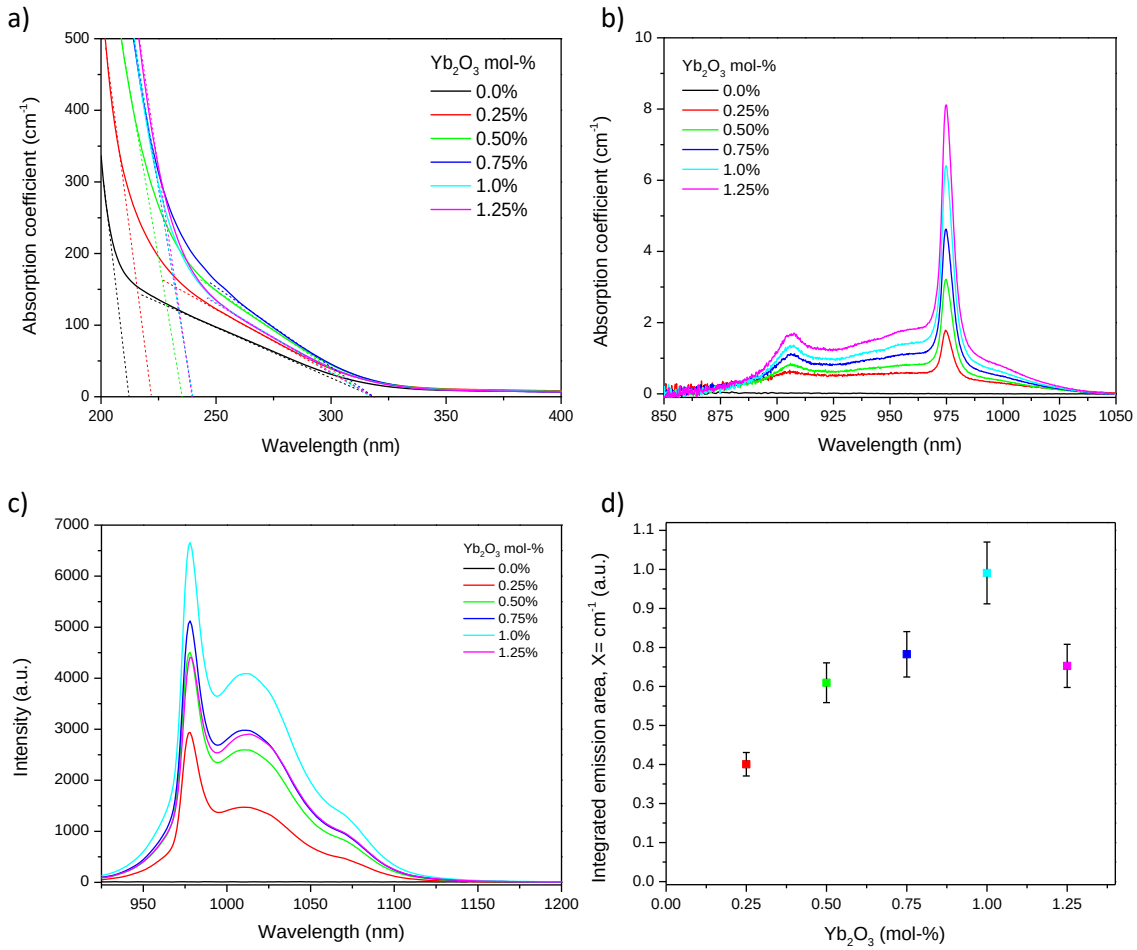

Figure 3: (a) Absorption coefficient of 200 µm thick samples around the UV absorption edge with tangents drawn for the optical band gap and Pt^{4+} related absorption band (b) Absorption coefficient around the Yb^{3+} absorption band (c) and Yb^{3+} emission intensity when excited at 240 nm (d) The normalized area under the emission curves as a function of the Yb^{3+} concentration

One can see that the UV absorption threshold has two different components, one that changes in correlation with the Yb^{3+} concentration and one that appears to be independent of Yb^{3+} concentration. The optical bandgap of the non-doped glass is found at 212 nm. A higher contribution of the Yb^{3+} ions is visible through an increased O^{2-}-Yb^{3+} charge transfer band intensity. In phosphate host lattice, this band is expected to be centered at around 210 nm.[22] The second band with intercept at 330 nm does not shift nor does correlate with the Yb^{3+} concentration. This band is caused by Pt^{4+} contamination

from the crucible based on its location and composition-independent behavior.[23, 24] Figure 3b displays the Yb^{3+} absorption coefficient for the characteristic $^2F_{5/2} - {}^2F_{7/2}$ transition of the Yb^{3+} ion. The shape and intensity of the absorption is consistent with previous report on borosilicate glasses doped with Yb^{3+}.[18] As can be seen in the Figures 3c and 3d, the emission intensity increases up to 1.0% Yb_2O_3 before it decreases for 1.25% due to concentration quenching. Similar Yb^{3+} threshold concentrations corresponding to $0.5x10^{21}$ ions cm^{-3} have been reported in other borosilicate glasses.[25]

In-vitro dissolution in simulated body fluid was performed for up to 2 weeks on the glass doped with 1 mol% of Yb_2O_3. Here 75 mg of glass powder (150-250 µm) immersed in 50 mL of SBF solution at 37 °C in an incubator rotating at 100 rpm to have a laminar flow. It is noteworthy that the behavior of the 1 mol% Yb2O3-doped glass in SBF is similar to that seen for the undoped glass [26]. As expected, the immersion of the borosilicate glass in SBF leads to an increase in the pH (Figure 4). This is due to ion exchange between Na^+ and H^+, as well as the leaching of cations in the immersion solution, as accepted during the dissolution of bioactive glasses within the silicate and borosilicate systems.[26] Ion release was further confirmed via Inductively Coupled Pasma – Optical Emission Spectroscopy (ICP-OES) analysis. Si and B that constitute the glass structure backbone were found to leach out into the immersion solution especially during the first 72 hours. At longer immersion time, the release of those ions slows down indicating that the soluble silica is first released in the solution while the strongly bonded silica remains in the network and re-polymerizes to form the SiO_2-rich gel layer. Boron is initially released from the surface. Boron does not participate in the hydrated layer formation. However, as the dissolution is diffusion based, this element is also released but at a slower rate at long immersion time. The Ca release is also found to rapidly leach out into the solution and levels off at immersion longer than 72 hours. The phosphorus in the SBF is found to decrease in concentration. As expected from this glass composition, the release of Ca and decrease in P can be associated with the precipitation of a reactive layer, expected to be hydroxyapatite according to [27]. It is noteworthy that the behavior of the 1 mol% Yb_2O_3-doped glass in SBF is similar to that seen for undoped glass in [26],

indicating that the addition of Yb2O3 up to 1.0 mol% does not modify the bioresponse of the glass. An hydroxyapatite layer is expected to form at the surface of the glass upon immersion in SBF.

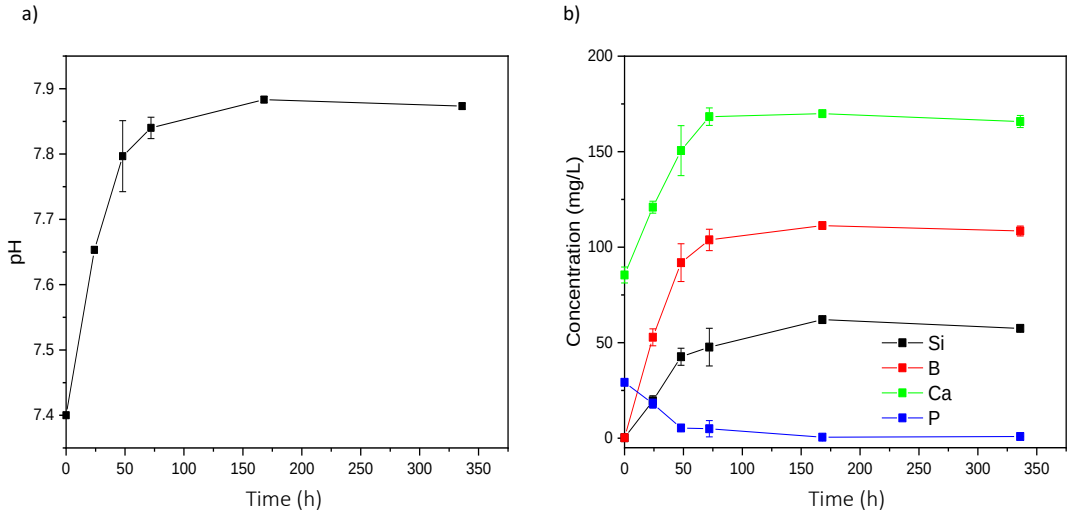

Figure 4: In vitro dissolution in simulated body fluid (a) pH of the solution (b) Si, B, Ca and P concentration as a function of immersion time

ii. Fiber characterization

We now investigate the properties of the core-clad borosilicate fibers prepared following the protocol exposed in Figure 1. Optical fibers were manually cleaved and the resulting cross-sections were imaged through an optical microscope (Figure 5). Both the rectangular and round fibers appear to have smooth and defect-free core-cladding interfaces based on multiple images taken in different positions along the z-axis. Furthermore, the general shape of the rectangular fiber has been well preserved, albeit with some rounding in the external corners. Similarly, the round fiber exhibits a well-preserved general aspect. The slight off-centering of the core and the swirls near the core-clad interfaces emanates from the graphite impinging drill used for elaboration.

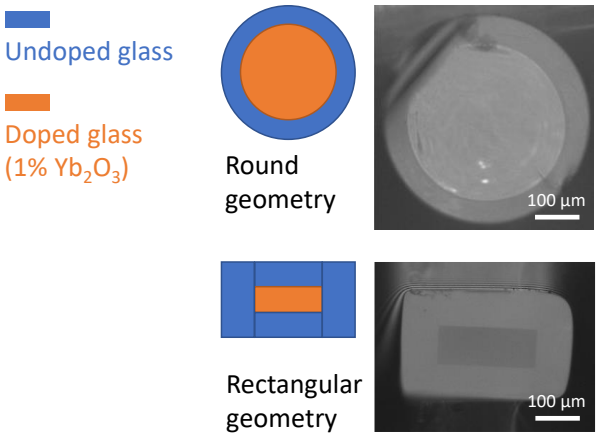

Figure 5: Schemes and optical microscope images of the prepared fibers cross-sections: round core-clad and rectangular fibers (the contrast dissimilarities observed between the core and clad are not related to chemical composition but to external reflections captured by the optical microscope).

To detect buried porosity otherwise not accessible using optical microscopy or SEM, X-ray micro-computed tomography (micro-CT) was undertaken on multiple fiber sections. Tomography is a non-destructive technique providing insights into the 3D spatial distribution, morphology and orientation of porosity within the sample with a micrometer scale voxel resolution. Tomography was performed on bundles of short (2-4 cm) fiber sections taken from different parts of the as-drawn fiber. Figure 6 shows computational tomography imaging resulting from a bundle of round core-clad fibers (Figure 6a) and rectangular core-clad fibers (Figure 6b), including three pictures of a single fiber taken at different axial positions along its axis.

The image slices were extracted from the imaged volumetric imaging data (~20 mm^3 per bundle). The grey level correlates with the X-ray absorption coefficient, i.e. composition, of the glass (the light color being related to the presence of ytterbium). The fiber parts were selected at different points along the drawn fiber (~10 m) in order to gauge the internal homogeneity in geometry, especially at the core-cladding interfaces. In the case of round fibers, the ratio of core and cladding diameters varies slightly, indicating that the impingement method does not produce perfectly cylindrical hole to be filled with

the doped core glass. Moreover, areas appearing darker nearby the interfaces may be related to inhomogeneous glass composition. Nevertheless, in the limit of resolution of the tomography voxel (order of 5 µm), the data suggest together that the impingement method, albeit improvements to prevent glass mixing, can be used to prepare round core-clad multimode fibers for research purposes. Tomography was also performed on the rectangular fiber bundle clearly evidencing the homogeneity in geometry and composition of the samples, along with the absence of detectable defects at core-cladding interface within the resolution of the instrument.

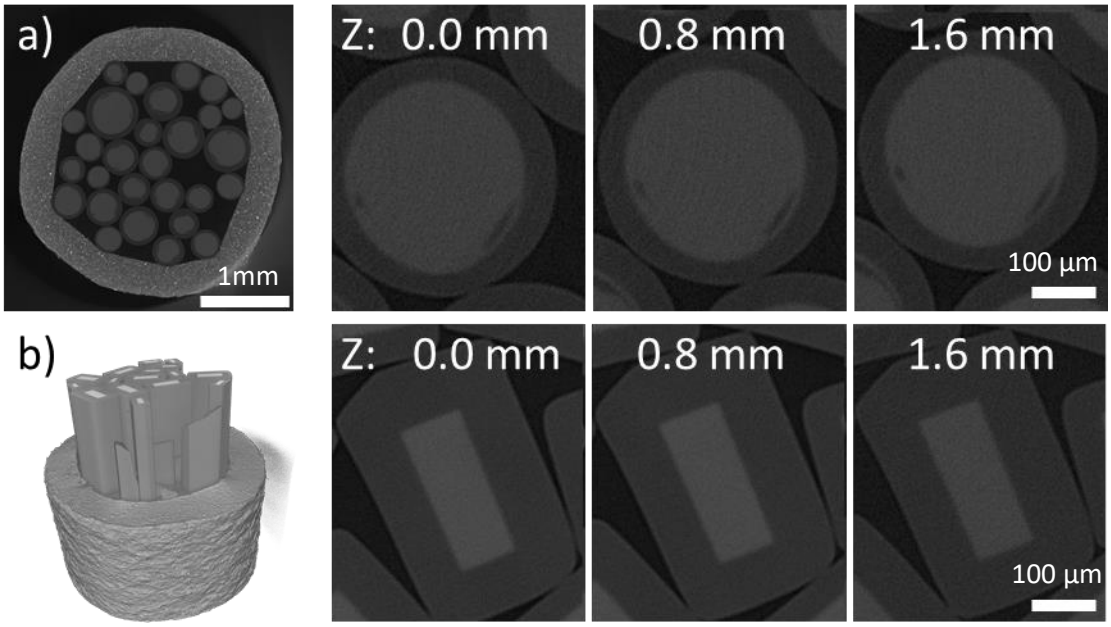

Figure 6: Micro-CT images and 3D model of the fiber bundles studied. A 2D image of the round fiber bundle encased in plastic shell, scale bar 1 mm (a). A 3D model of the rectangular fiber bundle (b). The three pictures are taken at different points along a single fiber, at 0.0/0.8/1.6 mm for both round and rectangular fibers.

The XRD patterns of the fibers (Figure 7a) depict broad bands, except for the aluminum metal peak originating from the sample holder, suggesting that the fibers are free from crystals. The XRD patterns appear to have two amorphous contributions with one prominent centered at around 30° and the

other, smaller one at around 45° meaning that the bands are a natural result of the bond length distributions in the glass.[17, 28]

The structure of the bulk glass, of the glass fiber preforms during the stacking process and of the drawn fiber was verified by Raman spectroscopy (Figure 7b). Extended Raman spectra analysis has been reported in more detail in [18]. The 400 to 700 cm^{-1} range is due to general Si-O-Si vibrations with bands between 520 and 600 cm^{-1} being related to vibrations of Q^3 units (Q^n with n being the number of bounded oxygen in Si-O-Si network), 590 to 650 cm^{-1} to Q^2 units and band at 700 cm^{-1} to Q^1 units. The 800 to 1200 cm^{-1} range is due to $Si\text{-}O^-$ bonds, where oxygen is a non-bridging oxygen (NBO type center). The most prominent bands at 940 cm^{-1} and 1050 cm^{-1} are due to Q^2 and Q^3 silicon tetrahedra, respectively.

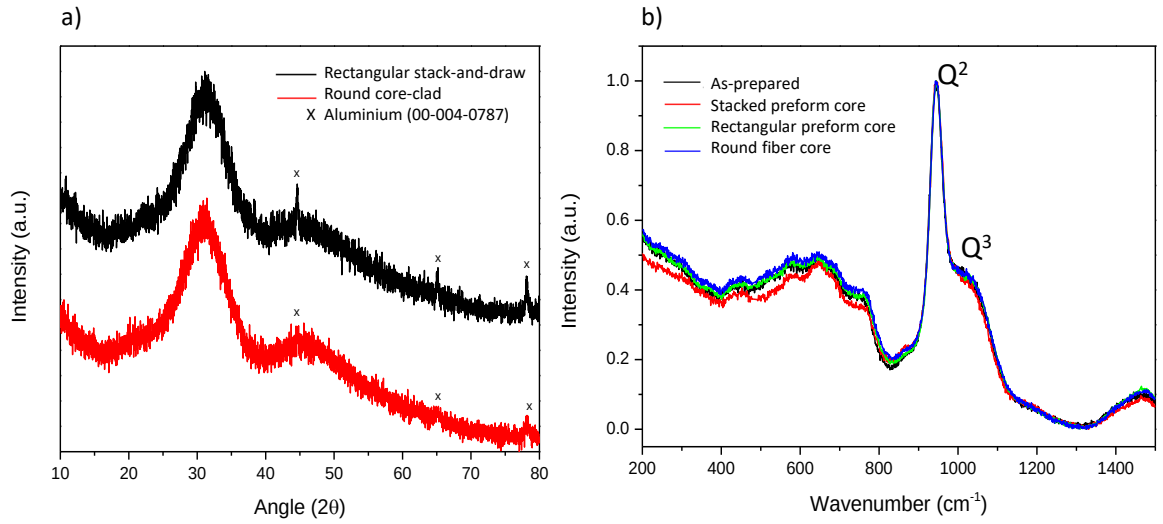

Figure 7: (a) XRD patterns of the round and rectangular round core-clad fibers (the peaks observed in the patterns are from the aluminum sample holder) and (b) normalized Raman spectra of the glass in various stages of processing

In order to measure and quantify possible Yb^{3+} ion diffusion from the doped core to the undoped cladding, the Yb^{3+} emission was mapped using an epifluorescent excitation near the core-cladding interface (Figure 8a). The boxes in Figure 8a correspond to the measured area of Figure 8b. In Figure

8b, the color represents the integrated Yb^{3+} emission area normalized to the maximum value and correlates directly with the Yb^{3+} ion concentration in the glass. Mapped areas are taken from opposite edges of the fiber core to capture the emission interface thickness around the core. One can observe that the Yb^{3+} luminescence remains constrain to the core. The luminescence drops significantly over an average thickness of 5 µm from the interface, which coincides with the approximate spot size of the excitation laser, meaning that the actual diffusion thickness is lower than 5µm.

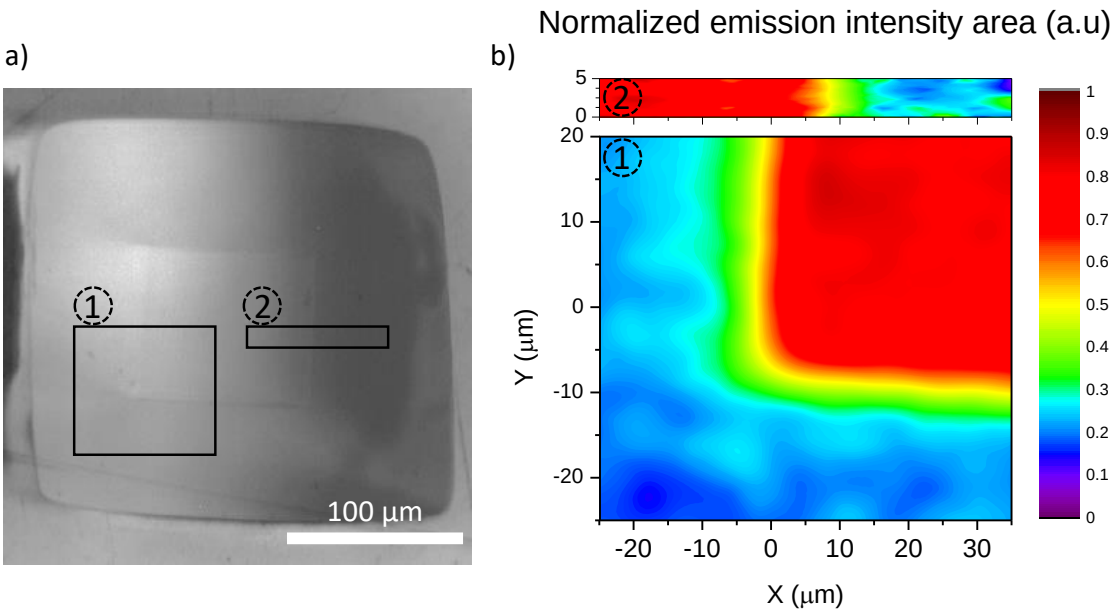

Figure 8: Optical image of a fiber with (a) areas highlighted in boxes mapped in (b) for normalized Yb^{3+} emission intensity area from 990 nm to 1100 nm of the $^2F_{5/2} - {}^2F_{7/2}$ transition when excited at 980 nm

Further evidence of Yb^{3+} ion confinement to the core can be found in Figure 9 that shows the SEM image and an Energy Dispersive Spectroscopy (EDS) mapping of another fiber (Figure 9a) along with an elemental line scan following the white arrow (Figure 9b). The atomic percentages were converted to corresponding glass constituent compounds with elements assumed present in nominal oxidation states and with boric oxide accounting for excess oxygen (as boron could not be detected directly) especially considering that EDS is a semi-quantitative method. Figure 9a confirms that the core is well defined with sharp edges and corners that did not deform during drawing. The line scan in Figure 9b

confirms that the ytterbium remains confined in the core. The elemental composition is largely consistent with nominal compositions, with no large spatial variations.

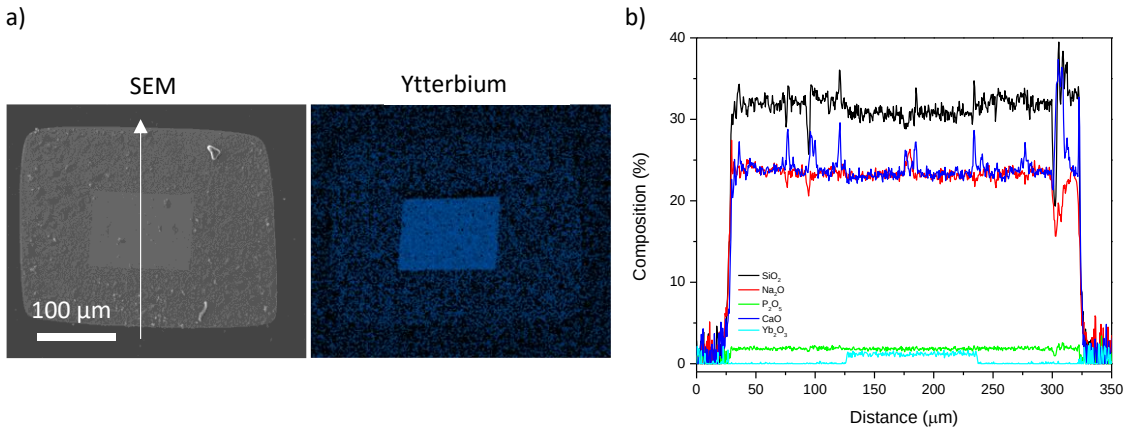

Figure 9: (a) SEM image and (b) EDS line scan along the arrow in the SEM image (boron was not included in the analysis due to low EDS sensitivity for boron)

iii. Fiber stability in simulated bioactive medium

The obtained fibers were then tested to probe their stability and response in a simulated bioactive fluid. The optical response of a 3-cm-long piece of fiber with 1-cm being immersed in SBF was investigated using a setup detailed in Figure 2. Transmission measurements were taken immediately after immersion (0 hours) and at 1, 2, 3, 6, and 9 hours. The optical response of the fiber immersed in simulated body fluid for up to 9 h is shown in Figures 10 for both geometries.

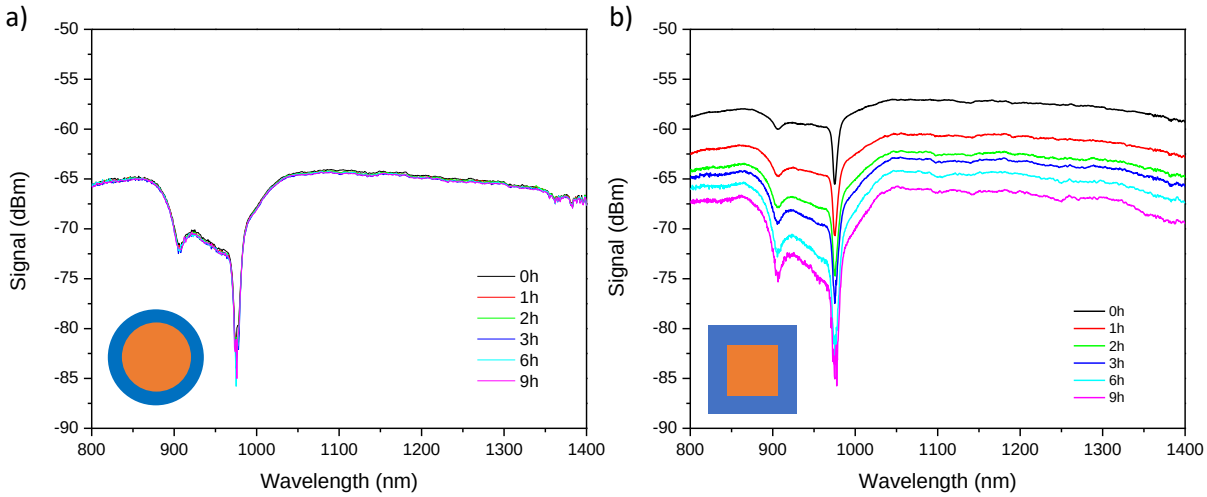

Figure 10: Transmitted optical power through 1-cm piece of fiber in SBF as a function of time for (a) round core-clad and (b) rectangular core-clad geometries

After a 9 hours immersion, the losses of the rectangular fiber increase whereas the round fiber transmission remains nearly constant. In the round fiber, the light is confined in the core and the cladding is sufficiently thick to act as a sacrificial layer/insulator preventing the transmitted light and the formed surface defects from interacting. Figure 11 shows the degradation of the round core-clad fiber after SBF immersion for a set period. The degradation is confined to the outer layer leaving the core intact. The reaction layer has progressed linearly from the outside but it did not reach the core due to the thickness of the cladding layer (Figure 11c).

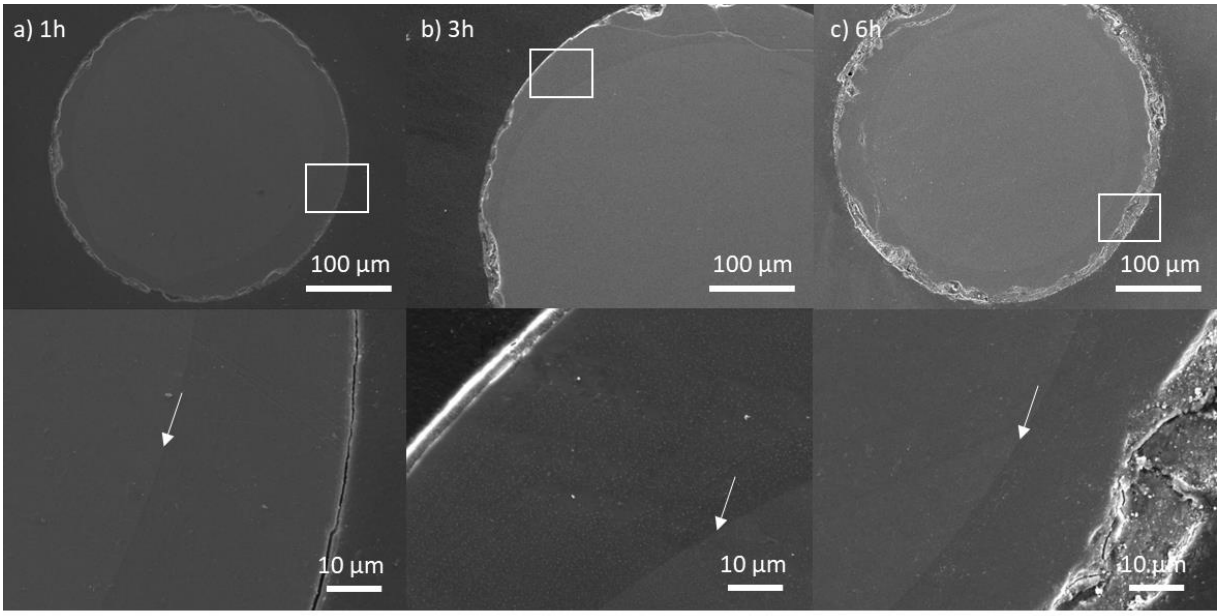

Figure 11: SEM images of the round core-clad fiber after (a) 1h (b) 3h and (c) 6 hours in SBF. Lower pictures are zoomed of the indicated boxed area. Arrows indicate core-cladding interface (samples immersed in epoxy resin).

On the contrary, as observed on SEM pictures (Figure 12), the rectangular core-clad fiber appears to be more sensitive to the aqueous medium, suggesting that the cladding appears to offer much less protection than the round cladding. The degradation behavior of the rectangular fiber is markedly different from that of the round fiber, the corrosion being extremely aggressive. The corrosion in the corners has almost reached the core while the sides are still remarkably intact. In addition, the corrosion appears to be largely independent of the stacking lines, i.e. the location and direction of interfaces between the original bulk glass slabs as degradation can be seen on the 4 corners.

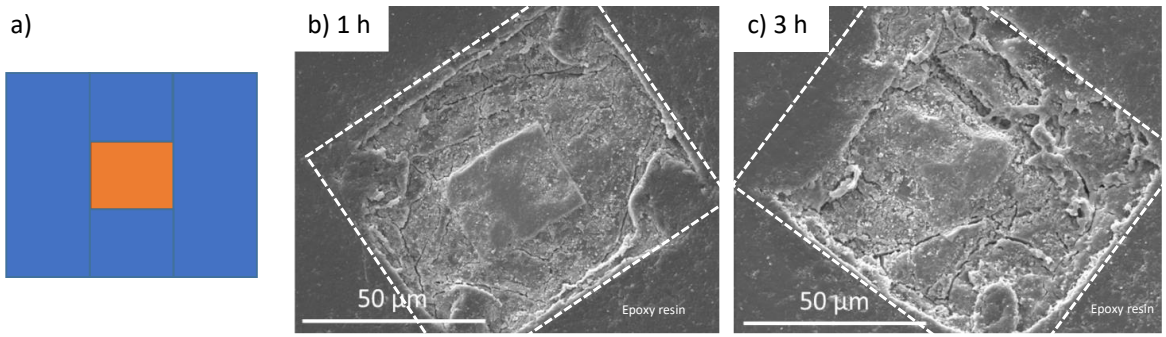

Figure 12: (a) Schematic diagram of the stacked fiber and (b) SEM images of the rectangular core-clad fiber prepared with the stack-and-draw technique after 1 hours and (c) 3 hours (samples immersed in epoxy resin). Dotted lines indicate the initial fiber perimeter.

A key aspect in this process is the stress corrosion cracking,[29, 30] a complex process where stresses in the glass contribute to chemical reactions. In general, the glass is more chemically active when under tensile stress and thus reacts more with water. The cause of the preferential corner corrosion could be found in the formation of microcracks and stress corrosion cracking as it was found that mechanical stress residues and induced microcracks accelerate significantly the dissolution process.[31] If microcracks or residual tensile stresses are present and the glass does not self-inhibit dissolution by forming hydration layers, then the dissolution reaction proceeds at a faster rate relative to a pristine glass surface.

Optical images of rectangular preform and resulting fibers were taken under polarized light to highlight stress concentration (Figure 13). In Figures 13a and 13b, the preform appears very homogenous, without any remaining stress concentrations from the stacking. Unlike preform, the picture of the rectangular fiber (Figure 13d) reveals a noticeable stress concentration within its side parts. The stress present in the glass is observed as fringing, which point to high stress concentrations that are perpendicular to the fiber outer surface (Figure 13d). Stress is at its strongest in the external corners

of the fibers, in agreement with the effects seen in Figure 12. Stress fringes in the round fiber (Figure 13e) are markedly different from the ones in the rectangular fiber as they are localized at the core-cladding interface, in parallel to the interface, not perpendicularly like with the rectangular fiber. Such a difference may reveal a significant discrepancy of the thermal gradients applied within the two types of fibers during the drawing process.

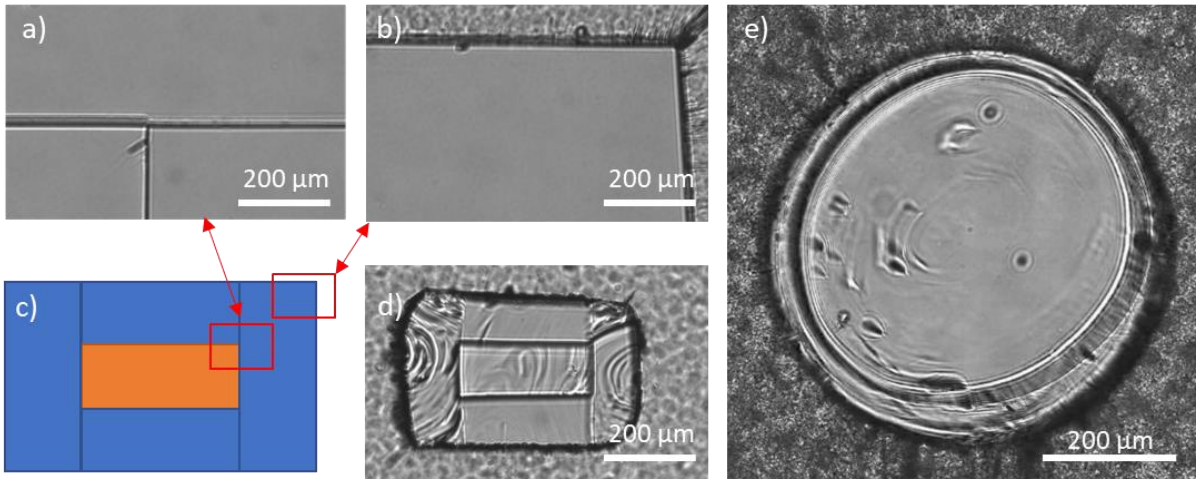

Figure 13: (a) Core-cladding interface and (b) cladding corner of a stacked rectangular preform with (c) a schematic diagram showing the locations of both pictures relative to fiber cross-section. Optical microscope images under polarized light of (d) Image of the drawn fiber and (e) round fiber. Images taken from samples in epoxy and polished to 400 µm in thickness. Rotating linear polarizers, lighting and focus were adjusted to maximize visibility of the fringes.

Attenuation measurements were performed at different visible-NIR wavelengths by the cutback method on initial 1-meter-long sections for both the round and rectangular fibers (Figure 14). Minimum loss is measured around 750-800 nm. Above this range of wavelengths, the Yb^{3+} absorption tail takes effect and the core begins to absorb light (Figure 3b). At lower wavelengths towards the blue parts of the spectrum, Rayleigh scattering affects the transmission.

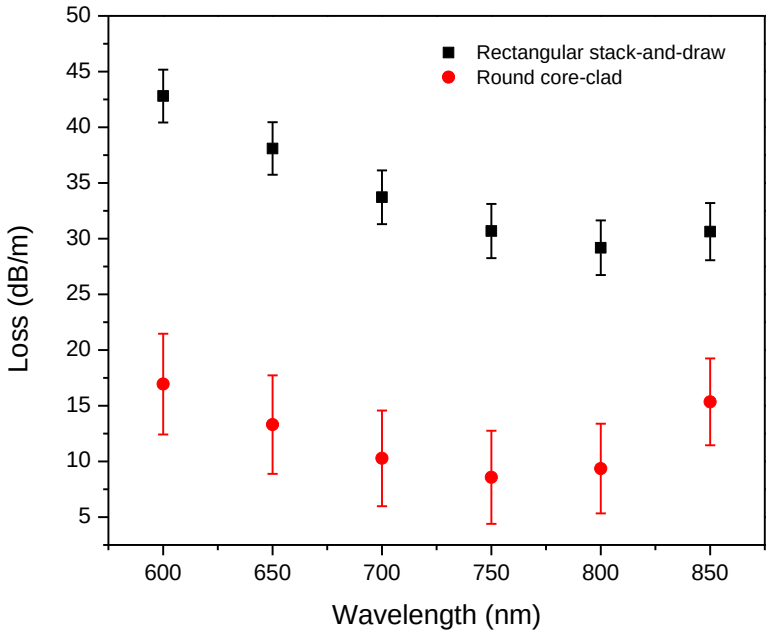

Figure 14: Optical loss of the core-clad fibers measured by the cutback method

Considering the round fiber first, loss shows a minimum of ~8 dB.m^{-1} at 750 nm. Although minimum loss remains relatively high for practical applications, at this stage it is at an expected level. Indeed, the preform elaboration method developed internally (Figure 1) leads to core-clad interface with remaining defects and no dedicated purification protocol other than the use of high-purity precursors was introduced at this stage.

In comparison to round fibers, the loss measured on the rectangular geometry is really high, in the order of 30 dB/m at 800 nm. In a first approach, one could relate the high loss to the rectangular shape of the core. Yet, comparative studies performed on fused silica optical fibers showed that light leakage do not significantly depend on the geometry of the fiber. On the contrary, the overall attenuation depends on the modes excited/guided in the fiber as low order modes suffer from lower attenuation, whereas high order modes which have a significant part of their energy spreading in the cladding, are much more attenuated.[32, 33] One has to keep in mind that, in our experiments, both round and rectangular fibers are highly multimode. For example, about 5000 linearly polarized (LP) modes are

expected to be guided in the round fiber shown in Figure 5 (core diameter = 330 µm), with Yb_2O_3 concentration of 1 mol-% (numerical aperture = 0.14) at λ = 980 nm. We must notice that light injection could be performed in a non-strictly consistent manner during cut back measurements in between the two types of fibers, resulting in an excited modal population different in the two types of fibers and thus in different overall loss. Equal power distribution in all modes orders ("modal equilibrium") should be achieved for mode-dependent loss mitigation.

Another point to be considered is that the core areas are significantly different in the round and in the rectangular fibers. As can be seen in Figure 5 for example, the area of the core of the round fiber is roughly twice that of the rectangular one. As the smaller dimension of the rectangular fiber (130 µm) is only slightly larger than the core diameter of the MM fiber used to launch light in this fiber (105 µm, see Figure 2), some input light may have coupled in the cladding, resulting in a distorted measurement. Yet, this difference in area is not sufficient to explain that the loss of the two fibers differ by orders of magnitude. In Figure 13d, noticeable stresses were visible even in the fiber core. As tensile stresses change the refractive index of a fiber [34] we can deduce that the fiber core in the rectangular fiber does not have a homogenous refractive index. Moreover, the stress distribution varies along the axial direction z, so that the index profile varies along z. These changes in the index profile may result in intense mode coupling. Thus, part of the guided energy can couple to higher order modes (leaky modes), resulting in high losses. Parametric study of the loss in these newly developed fibers, involving core geometry and diameter, specific numerical aperture and taking mode coupling into account will be the scope of a further detailed study.

A deeper characterization on the as-drawn fibers was performed to compare their optical properties. Figures 15a and 15b show NIR images (Yb^{3+} emission intensity) of the round and rectangular fibers respectively, when a 980 nm laser beam is launched from a multimode fiber. The round fiber scattering consists of bright defects that are localized at its surface, very similar to defects found in bent fibers,[35] indicating that the defects have formed from the fiber handling and too tight bending. We also see

some internal emission coming from the inside of the round fiber. In Figure 15a we notice the occurrence of small defects lying within the core of the round fibers. This is reinforced by the observation made by X-ray microtomography (Figure 6a). This would support the idea that these enclaves are the sources of the sharp light scattering decay observed on the round fiber, along with bending-related surface defects.

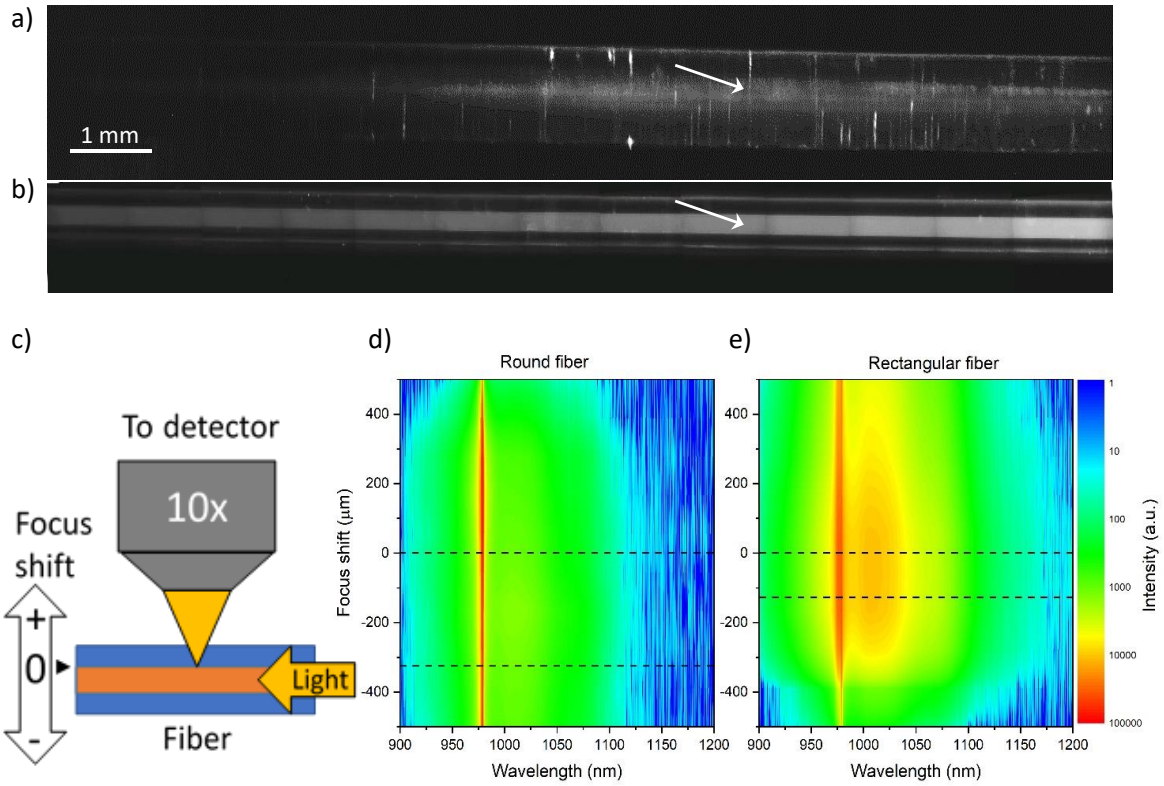

Figure 15: (a) Round and (b) rectangular core-clad fiber imaged in NIR while guiding 980 nm laser beam. Both images are stitched from multiple images, brightness and contrast increased equally in software for better visualization. White arrows indicate the measurement sites. (c) Schematic of the measurement setup. (d, e) Emission spectrum as a function of focus shift perpendicular from the fiber. Positive values correspond to focus moving towards the reader. Dashed lines indicate fiber core position.

The rectangular fiber in Figure 15b shows an entirely different picture when it comes to off-axis scattering. The entire core is seen glowing brightly and homogenously along the measured fiber length. This behavior is presumed to originate from the light mixing rod effect homogenizing the excitation beam through randomized reflections and then when it encounters a stress-related refractive index variation, the light beam has the opportunity to couple in leaky modes and then to propagate away from the core. The Yb^{3+} emission is also affected and the significant fraction of the light is no longer confined in the core.

Further demonstration of this can be seen in Figures 15c, where the emission spectrum of these two fibers is measured as a function of the focus shift perpendicular to the fiber. The round fiber has a very sharp excitation peak visible with a mild emission at the Yb^{3+} emission wavelengths, indicating that the scattering of the round fiber is dominated by the scattered excitation light (Figure 15d). A different case is seen for the rectangular fiber, which has a much more intense emission above 1000 nm, demonstrating that a larger portion of the light originating from Yb^{3+} emission extends beyond the physical dimensions of the fiber (Fiber 15e).

Conclusion

In the current report we demonstrate our ability to develop bioactive-based glass fibers with various geometries. Firstly we thoroughly characterized the physicochemical, photoluminescence and dissolution properties of the selected undoped and Yb-doped borosilicate glasses. Following, we expose two experimental protocols dedicated to the fabrication of core-clad bioactive borosilicate preforms and fibers, both with round and rectangular cross-section profiles. Using X-ray microtomography along with fluorescence spectroscopies and electronic microscopy analysis, fibers are found to exhibit good quality interface between the core and cladding, with very limited ytterbium diffusion from the core. Upon dissolution rate study of the fibers in simulated body fluid, supported with electronic microscopy, we show that the biodegradation behavior of the fibers is significantly

altered by changing the fiber external cross-section profile. Rectangular fibers suffer from much higher losses and accelerated degradation compared to circular ones, the differences being due to residual tensile stresses generated during fiber drawing, resulting in inhomogeneous refractive index in fiber core, leading to higher losses, and accelerated degradation at their corner. The stack-and-draw technique combined with chemical direct-bonding offer an alternative for the fabrication of preform build-up with complex shapes. The method was applied for instance recently for multimodal imaging,[36] providing the fact that, due to intrinsically superior fiber loss, the targeted application does not require extra-long devices. Similarly, here we show that the stack-and-draw rectangular fibers result in an interesting diffusing fiber source without the need for an additional surface treatment (as chemical etching or particles deposition).[37] Finally, as shown here, geometry also plays a critical role on the biodegradation behavior of a bioactive glass. In that perspective we believe the enclosed results may open up alternatives for developing bioactive fiber-based optical components where fine or differential glass dissolution rates would be needed.

Acknowledgments and support

The authors would like to acknowledge Regina Gumenyuk from Tampere University for the fruitful discussion. Academy of Finland Flagship Programme of Photonics Research and Innovation and Academy Project [grant numbers PREIN-320165]; French Region Nouvelle-Aquitaine [grant number 2019-1R1MO1]; LIGHT S&T Graduate Program in PIA3 Investment for the Future Program [grant number ANR-17-EURE-0027]

Data availability statement

The raw/processed data required to reproduce these findings cannot be shared at this time due to technical or time limitations.

References

1. Kociszewski L, Buźniak J, Stępień R. "Optical devices and sensors made of special-purpose fibers" Proc. SPIE 0867 Opt Devices Adverse Environment 1988.
2. Romaniuk R, Kociszewski L, Stepien R, Butniak J. "Mosaic optical fibers" Proc. SPIE 1085 Opt Fib Appl V 1990.
3. Birks T A, Knight J C, Russell P. "Endlessly single-mode photonic crystal fiber" Opt. Lett. 1997 22(13) p. 961-963.
4. Russell P. "Photonic-crystal fibers" J. Lightwave Technol. 2006 24(12) p. 4729-4749.
5. Chillcce E F, Cordeiro C M, Barbosa L C, Brito Cruz H C. "Tellurite photonic crystal fiber made by a stack-and-draw technique" J. Non-Cryst. Solids 2006 352(32) p. 3423-3428.
6. Jiang X, Joly N Y, Finger M A, Babic F, Wong G, Travers J C, Russell P. "Deep-ultraviolet to mid-infrared supercontinuum generated in solid-core ZBLAN photonic crystal fibre" Nat Photonics 2015 9(2) p. 133-139.
7. Tyagi H K, Lee H W, Uebel P, Schmidt M, Joly N, Scharrer M *et al.* "Plasmon resonances on gold nanowires directly drawn in a step-index fiber" Opt. Lett. 2010 35(15) p. 2573-2575.
8. Strutynski C, Meza R A, Teulé-Gay L, El-Dib G, Poulon-Quintin A, Salvetat J-P *et al.* "Stack-and-draw applied to the engineering of multimaterial fibers with non-cylindrical profiles" Adv. Funct. Mater. 2021 31(22) 2011063.
9. Heng S, McDevitt C A, Kostecki R, Morey J R, Eijkelkamp B A, Ebendorff-Heidepriem H *et al.* "Microstructured optical fiber-based biosensors: reversible and nanoliter-scale measurement of zinc ions" ACS Appl. Mater. Interfaces 2016 8(20) p. 12727-12732.
10. Falah A A S, Wong W R, Mahdiraji G A, Adikan F R M. "Single-mode D-shaped photonic crystal fiber surface plasmon resonance sensor with open microchannel" Opt. Fiber Technol. 2022 74 103105.
11. Heyvaert S, Ottevaere H, Kujawa I, Buczynski R, Thienpont H. "Stack-and-draw technique creates ultrasmall-diameter endoscopes" Laser Focus World 2013 49(12) p. 29-35.

12. Gonzales R E R, Garcia J F, Filho C, Barbosa L. C. "Rigid endoscopes of the microstructured optical fiber" Proc. 2018 SBFoton IOPC 2018 p. 1-4.
13. Hench L L. "Bioceramics: from concept to clinic" J. Am. Ceram. Soc. 1991 74(7) p. 1487-1510.
14. Gallichi-Nottiani D, Pugliese D, Boetti N G, Milanese D, Janner D. "Toward the fabrication of extruded microstructured bioresorbable phosphate glass optical fibers" Int. J. Applied Glass Sc. 2020 11(4) p. 632-640.
15. Mussavi Rizi S H, Boetti N G, Pugliese D, Janner D. "Phosphate glass-based microstructured optical fibers with hole and core for biomedical applications" Opt. Mater. 2022 131 112644.
16. Kokubo T, Ito S, Huang Z T, Hayashi T, Sakka S, Kitsugi T *et al.* "Ca, P-rich layer formed on high-strength bioactive glass-ceramic" J. Biomed. Mater. Res. 1990 24(3) p. 331-343.
17. Fabert M, Ojha N, Erasmus E, Hannula M, Hokka M, Hyttinen J *et al.* "Crystallization and sintering of borosilicate bioactive glasses for application in tissue engineering" J. Mater. Chem. 2017 B5(23) p. 4514-4525.
18. Hongisto M, Danto S, Ghena M, Iancu D, Ighigeanu D, Mihai L *et al.* "Response of various Yb^{3+}-doped oxide glasses to different radiation treatments" Materials 2022 15(9) 3126.
19. Choi J H, Margaryan A, Shi F. G. "Dependence of thermo-mechanical and mechanical properties of novel fluorophosphate glass on various rare earth dopants" J. Mater. Sc. 2008 43(3) p. 1109-1113.
20. Lin Y-T, Smith N J, Banerjee J, Agnello G, Manley R G, Walczak W J *et al.* "Water adsorption on silica and calcium-boroaluminosilicate glass surfaces - Thickness and hydrogen bonding of water layer" J. Am. Ceram. Soc. 2021 104(3) p. 1568-1580.
21. Amma S-I, Kim S H, Pantano C G. "Analysis of water and hydroxyl species in soda lime glass surfaces using attenuated total reflection (ATR)-IR spectroscopy" J. Am. Ceram. Soc. 2016 99(1) p. 128-134.
22. Nakazawa E. "Charge-transfer type luminescence of Yb^{3+} ions in $LuPO_4$ and YPO_4" Chemical Phys. Lett. 1978 56(1) p. 161-163.

23. Boiruchon D, Desevedavy F, Chenu S, Strutynski C, Smektala F, Gadret G *et al.* "Investigation of the Na_2O/Ag_2O ratio on the synthesis conditions and properties of the $80TeO_2–10ZnO–[(10−x)Na_2O–xAg_2O]$ glasses" J. Non-Cryst. Solids 2019 525 119691.
24. Click C A, Brow R K, Ehrmann P R, Campbell J H. "Characterization of Pt^{4+} in alumino-metaphosphate laser glasses" J. Non-Cryst. Solids 2003 319(1-2) p. 95-108.
25. Yamashita T, Ohishi Y. "Cooperative energy transfer between Tb^{3+} and Yb^{3+} ions co-doped in borosilicate glass" J. Non-Cryst. Solids 2008 354(17) p. 1883-1890.
26. Tainio J M, Avila Salazar D A, Nommeots-Nomm A, Roiland C, Bureau B, Neuville D R *et al.* "Structure and in vitro dissolution of Mg and Sr containing borosilicate bioactive glasses for bone tissue engineering" J. Non-Cryst. Solids 2020 533 p.119893.
27. Erasmus E P, Sule R, Johnson O T, Massera J, Sigalas I. "In vitro evaluation of porous borosilicate, borophosphate and phosphate bioactive glasses scaffolds fabricated using foaming agent for bone regeneration" Sci. Rep. 2018 8 p. 3699.
28. Warren B E. "X-ray determination of the structure of glass" J. Am. Ceram. Soc. 1992 75(1) p. 5-10.
29. Wachtman J B, Cannon W B, Matthewson M J. "Mechanical properties of ceramics" In Mechanical Properties of Ceramics, 2^{nde} Edition, John Wiley and Sons 2009.
30. Gurney C, Pearson S. "The effect of the surrounding atmosphere on the delayed fracture of glass" Proc. Phys. Soc. B 1949 62(8) p. 469-476.
31. Yu J, Jian Q, Yuan W, Gu G, Ji F, Huang W. "Further damage induced by water in micro-indentations in phosphate laser glass" Appl. Surf. Sci. 2014 292 p. 267-277.
32. Kandilli C, Ulgen K. "Review and modelling the systems of transmission concentrated solar energy via optical fibres" Renew. Sust. Ener. Rev. 2009 13 (1) p. 67-84.
33. Dugas J, Sotom M, Martin L, Cariou J M. "Accurate characterization of the transmittivity of large diameter multimode optical fibers" Appl. Opt. 1987 26(19) p. 4123-4132.

34. Fonjallaz P Y, Limberger H G, Salathé R P, Cochet F, Leuenberger B. "Tension increase correlated to refractive-index change in fibers containing UV-written Bragg gratings" Opt. Lett. 1995 20(11) p. 1346-1348.
35. Chen Y, Cui Y, Gong W. "Crack propagation calculations for optical fibers under static bending and tensile loads using continuum damage mechanics" Sensors 2017 17(11) p. 2633.
36. Evrard M, Mansuryan T, Couderc V, Désévédavy F, Strutynski C, Dussauze M *et al.* "Highly nonlinear multimode tellurite fibers: from glass synthesis to practical applications in multiphoton imaging" Adv. Phot. Res. 2023 4 p. 2200213.
37. Cennamo N, Trono C, Giannetti A, Baldini F, Minardo A, Zeni L *et al.* "Biosensors exploiting unconventional platforms: the case of plasmonic light-diffusing fibers" Sensor Actuator B-Chemical 2021 337 129771.